AIAA JOURNAL
Vol. 45, No. 2, February 2007

Nonlinear Response of Axially Compressed Laminated Cylindrical Shell Panels

Scott T. Dennis*
U.S. Air Force Academy, Colorado Springs, Colorado 80840

DOI: 10.2514/1.25754

A kinematics-based geometrically nonlinear thin-shell approach is presented. Reddy–Levinson–Murthy displacements have cubic distributions through the shell thickness for the in-plane shell displacements and result in parabolic transverse shear strain. Strains are assumed to be small and of the order of θ^2, where θ^2 is a small quantity compared with unity. The nonlinearity allows moderate rotations by retaining terms of the order of θ^3 and larger in the strain-displacement relations. Each of the shell strains is nonlinear in displacement. A second, simpler, intermediate nonlinearity of the von Kármán type results by retaining all terms of the order of θ^2 and larger. The von Kármán type approach has displacement nonlinearity in the in-plane strains, yet is linear in displacement for the transverse shear strains. For solution of the shell equations, the finite element method using a 36-degree-of-freedom curved shell element is developed. The nonlinear response of axially compressed laminated cylindrical shell panels is examined and compared with existing experimental results. The influence of the nonlinear transverse strain-displacement terms of the moderate rotation approach is illustrated in a numerical simulation of an axially compressed unsymmetrically laminated cross-ply panel.

I. Introduction

THIN-WALLED shell structures loaded in compression are prevalent in aerospace applications and susceptible to instabilities and potentially sudden failure. Composites, with their attractive strength, stiffness, and weight characteristics, are being used increasingly in aircraft primary structure. Because of unique structural couplings, laminated geometries also present opportunities for tailoring these characteristics to suit requirements. Consequently, the buckling characteristics of composite shells continue to be studied by investigators seeking a more complete understanding of the shell's nonlinear response under a variety of loadings. Recently, for example, Hilburger et al. [1] identify an "imperfection signature" for laminated cylindrical shells that may allow for lower weight design methodology vs more typical approaches. Sheinman and Goldfeld [2] compare the Donnell, Sanders, and Timoshenko bifurcation buckling theories using composite cylindrical shells subjected to axial compression and torsion. Tudela et al. [3,4] examine transversely loaded composite shell panels that experience snap-through instability.

Unsymmetrically laminated geometries represent a special case of structural couplings and potential for unique applications. Weaver [5] discusses advantages of unsymmetrically stacked laminates for use in deployable structures. Diaconu and Weaver [6] use a nondimensional coupling parameter for unsymmetric laminates to show that flat plates with a high degree of coupling behave more as curved panels. Shultz and Hyer [7] apply bistable unsymmetric laminates to morphing structures.

Analytical and design challenges come with the structural advantages that composites offer. Axially compressed unsymmetric flat plates are examined by Majeed and Hyer [8] and they show how slight changes in the plate boundary conditions affect whether bifurcation buckling occurs. Additionally, in the special case of unsymmetrically laminated plate geometries [9–11] due to membrane-bending coupling, nonlinearity becomes important even in cases for which deflections are normally considered small. Recently, this has been found to be true in the case of laminated shells, as well [12].

The present paper develops a small-strain, elastic, geometrically nonlinear shell approach applicable to doubly curved laminated panels with arbitrary ply orientation stacking. Reddy–Levinson–Murthy [13–15] shell kinematics result in parabolic transverse shear strain and, therefore, stress through the shell thickness. The shell is assumed to be thin, such that an approximate state of plane stress exists (i.e., the transverse normal stress is approximately zero). However, transverse shear strains can be significant, due to the relative weakness in shear of many composite systems. A more complex parabolic transverse stress and strain distribution is preferred over a simpler Reissner–Mindlin approach, as the latter has well-known numerical challenges (e.g., shear locking in finite element solutions and the requirement of shear correction factors) [16,17].

Strains are assumed to be small and of the order of θ^2, where θ^2 is a small number compared with unity. The nonlinearity allows moderate rotations by retaining terms of the order of θ^3 and larger in the strain-displacement relations. Each of the shell strains is nonlinear in displacement. A second, simpler, intermediate nonlinearity of the von Kármán type results by retaining all terms of the order of θ^2 and larger. The von Kármán type nonlinearity results in nonlinear in-plane strain displacement, yet linear transverse shear strain displacement. The nonlinearity contrasts with the approaches used by Alwar and Narashimhan [18], Librescu [19], Schmidt and Reddy [20], and Dennis and Palazotto [21].

Starting with a description of the shell geometry, the development next motivates the nonlinearity by a comparison with the work of others. The strain-displacement relations are then presented. Once the orthotropic material is described, the shell potential energy is developed. A 36-degree-of-freedom (DOF) doubly curved element allows numerical solution. In view of the computational burden, parts of the finite element code were parallelized. This paper applies the approach to an axially compressed cylindrical shell and comparisons are made with representative laminates of the extensive experimental results of Wilkins [22,23] and Love and Brubaker [24]. Additionally, the influence of the moderate rotation terms is illustrated in a numerical simulation of an axially compressed, unsymmetrically laminated, cross-ply panel.

Received 12 June 2006; revision received 14 August 2006; accepted for publication 14 August 2006.

*Professor, Department of Engineering Mechanics. Senior Member AIAA.

II. Approach

A. Shell Geometry

Consider the doubly curved shell geometry shown in Fig. 1. Designate ξ_1, ξ_2, and ζ as orthogonal curvilinear coordinates, where the ξ_1 and ξ_2 axes are along lines of curvature at the shell middle surface (i.e., for $\zeta = 0$). Coordinate ζ varies along straight lines normal to the surface. The coordinate lines coincide with the principal directions of the shell and the principal radii of curvature are R_1 and R_2.

The position vector $\bar{\boldsymbol{R}}$ to any point of the shell is given by Eq. (1), where the position vector to any point on the shell middle surface is given by $\bar{\boldsymbol{r}}$, and $\bar{\boldsymbol{n}}$ is a unit vector normal to the middle surface.

$$\bar{\boldsymbol{R}} = \bar{\boldsymbol{r}}(\xi_1, \xi_2) + \zeta \bar{\boldsymbol{n}}(\xi_1, \xi_2) \tag{1}$$

The dot product of the shell position vector with itself gives the first fundamental form and the distance $\mathrm{d}s$ between any two points of the shell, given in Eq. (2).

$$\mathrm{d}s^2 = a_{11}\left(1 - \tfrac{\zeta}{R_1}\right)^2 \mathrm{d}\xi_1^2 + a_{22}\left(1 - \tfrac{\zeta}{R_2}\right)^2 \mathrm{d}\xi_2^2 + \mathrm{d}\zeta^2 \tag{2}$$

where a_{11} and a_{22} are elements of the middle surface metric. The parameters a_{11}, a_{22}, R_1, and R_2 are considered constants in this study.

The shell scale factors are then defined from Eq. (2) in Eq. (3); see Saada [25].

$$h_1 = \alpha_1\left(1 - \tfrac{\zeta}{R_1}\right), \qquad h_2 = \alpha_2\left(1 - \tfrac{\zeta}{R_2}\right), \qquad h_3 = 1 \tag{3}$$

where $\alpha_\gamma = \sqrt{a_{\gamma\gamma}}$ (no sum) and $\gamma = 1, 2$.

B. Geometric Nonlinearity

Starting with the Green strain expressions from Novozhilov [26], the geometric nonlinearity for the shell geometry just described is developed. Order-of-magnitude arguments on the components of the strains lead to moderate rotation nonlinearity. The resulting moderate rotation strain-displacement relations are similar to that seen in the open literature.

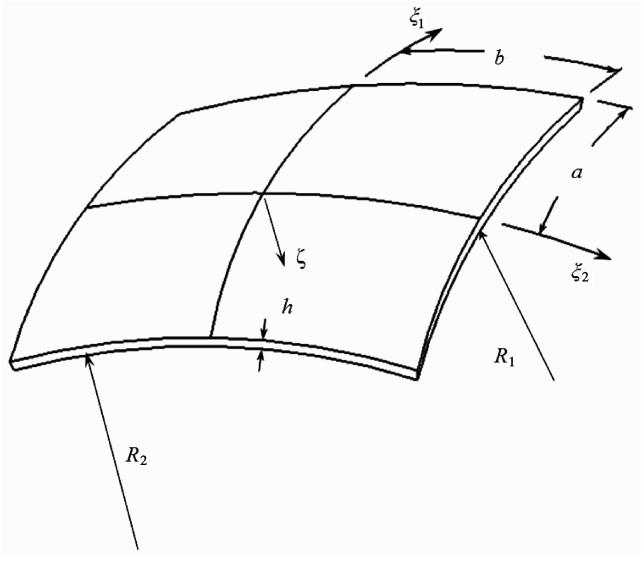

Fig. 1 Spherical shell panel geometry.

$$\begin{aligned}
\varepsilon_{11} &= e_{11} + \tfrac{1}{2}\left[e_{11}^2 + \left(\tfrac{1}{2}e_{12} + \omega_3\right)^2 + \left(\tfrac{1}{2}e_{13} - \omega_2\right)^2\right] \\
\varepsilon_{22} &= e_{22} + \tfrac{1}{2}\left[e_{22}^2 + \left(\tfrac{1}{2}e_{12} - \omega_3\right)^2 + \left(\tfrac{1}{2}e_{23} + \omega_1\right)^2\right] \\
\varepsilon_{33} &= e_{33} + \tfrac{1}{2}\left[e_{33}^2 + \left(\tfrac{1}{2}e_{13} + \omega_2\right)^2 + \left(\tfrac{1}{2}e_{23} - \omega_1\right)^2\right] \\
\varepsilon_{12} &= e_{12} + e_{11}\left(\tfrac{1}{2}e_{12} - \omega_3\right) + e_{22}\left(\tfrac{1}{2}e_{12} + \omega_3\right) \\
&\quad + \left(\tfrac{1}{2}e_{13} - \omega_2\right)\left(\tfrac{1}{2}e_{23} + \omega_1\right) \\
\varepsilon_{13} &= e_{13} + e_{11}\left(\tfrac{1}{2}e_{13} + \omega_2\right) + e_{33}\left(\tfrac{1}{2}e_{13} - \omega_2\right) \\
&\quad + \left(\tfrac{1}{2}e_{12} + \omega_3\right)\left(\tfrac{1}{2}e_{23} - \omega_1\right) \\
\varepsilon_{23} &= e_{23} + e_{22}\left(\tfrac{1}{2}e_{23} - \omega_1\right) + e_{33}\left(\tfrac{1}{2}e_{23} + \omega_1\right) \\
&\quad + \left(\tfrac{1}{2}e_{12} - \omega_3\right)\left(\tfrac{1}{2}e_{13} + \omega_2\right)
\end{aligned} \tag{4}$$

where the linear strain components e_{ij} in Eq. (4) are defined in Eq. (5)

$$\begin{aligned}
e_{11} &= \frac{1}{h_1}\frac{\partial u_1}{\partial \xi_1} + \frac{1}{h_1 h_2}\frac{\partial h_1}{\partial \xi_2}u_2 + \frac{1}{h_1 h_3}\frac{\partial h_1}{\partial \zeta}u_3 \\
e_{22} &= \frac{1}{h_2}\frac{\partial u_2}{\partial \xi_2} + \frac{1}{h_2 h_3}\frac{\partial h_2}{\partial \zeta}u_3 + \frac{1}{h_1 h_2}\frac{\partial h_2}{\partial \xi_1}u_1 \\
e_{33} &= \frac{1}{h_3}\frac{\partial u_3}{\partial \zeta} + \frac{1}{h_1 h_3}\frac{\partial h_3}{\partial \xi_1}u_1 + \frac{1}{h_2 h_3}\frac{\partial h_3}{\partial \xi_2}u_2 \\
e_{12} &= \frac{h_2}{h_1}\frac{\partial}{\partial \xi_1}\left(\frac{u_2}{h_2}\right) + \frac{h_1}{h_2}\frac{\partial}{\partial \xi_2}\left(\frac{u_1}{h_1}\right) \\
e_{13} &= \frac{h_1}{h_3}\frac{\partial}{\partial \zeta}\left(\frac{u_1}{h_1}\right) + \frac{h_3}{h_1}\frac{\partial}{\partial \xi_1}\left(\frac{u_3}{h_3}\right) \\
e_{23} &= \frac{h_3}{h_2}\frac{\partial}{\partial \xi_2}\left(\frac{u_3}{h_3}\right) + \frac{h_2}{h_3}\frac{\partial}{\partial \zeta}\left(\frac{u_2}{h_2}\right)
\end{aligned} \tag{5}$$

and the ω_i parameters are

$$\begin{aligned}
\omega_1 &= \frac{1}{2h_2h_3}\left[\frac{\partial}{\partial \xi_2}(h_3u_3) - \frac{\partial}{\partial \zeta}(h_2u_2)\right] \\
\omega_2 &= \frac{1}{2h_1h_3}\left[\frac{\partial}{\partial \zeta}(h_1u_1) - \frac{\partial}{\partial \xi_1}(h_3u_3)\right] \\
\omega_3 &= \frac{1}{2h_1h_2}\left[\frac{\partial}{\partial \xi_1}(h_2u_2) - \frac{\partial}{\partial \xi_2}(h_1u_1)\right]
\end{aligned} \tag{6}$$

where u_1, u_2, and u_3 are the displacements in the ξ_1, ξ_2, and ζ directions, respectively, and the scale factors h_i were defined in Eq. (3).

Next, assume the strains are small. That is, assume the strains are of the order of magnitude of θ^2, where θ^2 is a quantity that is small compared with one [see Eq. (7a)]. Additionally, assume the rotations of the shell panel normals for small strains of the shell middle surface and the rotations of the surface tangents, except rotation about the surface normal, are of the magnitude of θ [see Eq. (7b)]. The rotations about the surface normals are of the magnitude of θ^2 [see Eq. (7c)].

$$\varepsilon_{ij}, e_{ij} = \mathcal{O}(\theta^2) \tag{7a}$$

$$\left(\tfrac{1}{2}e_{13} - \omega_2\right), \qquad \left(\tfrac{1}{2}e_{23} + \omega_1\right), \qquad \left(\tfrac{1}{2}e_{13} + \omega_2\right) \qquad \left(\tfrac{1}{2}e_{23} - \omega_1\right) = \mathcal{O}(\theta) \tag{7b}$$

$$\left(\tfrac{1}{2}e_{12} + \omega_3\right), \qquad \left(\tfrac{1}{2}e_{12} - \omega_3\right) = \mathcal{O}(\theta^2) \tag{7c}$$

where $\theta^2 \ll 1$.

Retaining terms that are of the order of θ^3 and greater in Eq. (4) then gives the following simplified strain components, for which the terms that multiply the tracer I_1 are of the magnitude of θ^2 and the terms that multiply the tracer I_2 are of the magnitude of θ^3. A von Kármán type (VK) nonlinearity results if I_1 is set to one and I_2 is set to zero. If both I_1 and I_2 are set to one, a moderate rotation (MR) nonlinearity results that has additional nonlinearity in the transverse shear strains.

$$\varepsilon_{11} = e_{11} + \tfrac{1}{2}I_1(\tfrac{1}{2}e_{13} - \omega_2)^2 \qquad \varepsilon_{22} = e_{22} + \tfrac{1}{2}I_1(\underline{\tfrac{1}{2}e_{23} + \omega_1})^2$$
$$\varepsilon_{12} = e_{12} + I_1(\tfrac{1}{2}e_{23} + \omega_1)(\tfrac{1}{2}e_{13} - \omega_2)$$
$$\varepsilon_{13} = e_{13} + I_2[e_{11}(\tfrac{1}{2}e_{13} + \omega_2) + (\tfrac{1}{2}e_{12} + \omega_3)(\tfrac{1}{2}e_{23} - \omega_1) + e_{33}(\tfrac{1}{2}e_{13} - \omega_2)]$$
$$\varepsilon_{23} = e_{23} + I_2[e_{22}(\tfrac{1}{2}e_{23} - \omega_1) + (\tfrac{1}{2}e_{12} - \omega_3)(\tfrac{1}{2}e_{13} + \omega_2) + e_{33}(\tfrac{1}{2}e_{23} + \omega_1)] \tag{8}$$

$$\varepsilon_{33} = e_{33} + \tfrac{I_1}{2}[(\tfrac{1}{2}e_{13} + \omega_2)^2 + (\tfrac{1}{2}e_{23} - \omega_1)^2] \tag{9}$$

where tracers I_1 and I_2 are defined in the preceding paragraph.

The present approach considers terms such as the one underlined in Eq. (8), for example, to give a quantity when squared of the magnitude of θ^2 [see also Eq. (7b)]. That is, the two quantities in the parentheses that are underlined ($\frac{1}{2}e_{23}$ and ω_1) are approximately composed of a rotation of a shell surface tangent; Fig. 2 illustrates this. The rotation of a surface tangent (originally ξ_2, for example, shown in the top of Fig. 2) and a normal to the surface (originally ζ) are each composed of rotations ω_1 and e_{23}. The sum of ω_1 and $\frac{1}{2}e_{23}$ represents the rotation of the surface tangent, and this combination is seen in the in-plane strains ε_{22} and ε_{12}. The difference of ω_1 and $\frac{1}{2}e_{23}$ is the rotation of the normal, and this difference is seen in the transverse strains ε_{13}, ε_{23}, and ε_{33}. Similar results for a rotation of a surface tangent ξ_1 are illustrated in the bottom part of Fig. 2 [26].

This approach contrasts somewhat to the moderate rotation approaches presented by Schmidt and Reddy [20], Alwar and Narasimhan [18], Librescu [19], and Dennis and Palazotto [21]. Schmidt and Reddy neglect any e_{ij}^2 term, as each is of the order of θ^4. Their approach would square the underlined term of Eqs. (8) and then retain those quantities that are of the magnitude of θ^3 and greater (i.e., the $e_{23}\omega_1$ and ω_1^2 terms) and neglect the e_{23}^2 term. Alwar and Narashimhan present an approach similar to that shown in Eqs. (8) for the in-plane strains of the shell (ε_{11}, ε_{12}, and ε_{22}). However, their transverse strains are different, in that presently, Eqs. (8) retain more terms. Librescu retains only those terms that multiply I_1 in Eqs. (8) and, hence, his transverse shear strains are linear with displacement. Dennis and Palazotto retained all terms of Eqs. (4) for the in-plane strains, yet only retained the terms linear in displacement for the transverse shear strains.

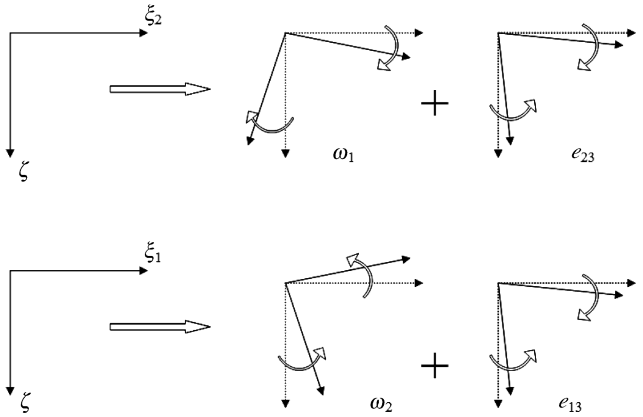

Fig. 2 Rotations of surface tangents and normals to the surface are composed of two components. Positive quantities for ω_1, ω_2, e_{23}, and e_{13} are shown.

The present approach considers each of the nonlinear displacement terms in the transverse shear strains to be of the magnitude of θ^3 and, hence, retains all of them. In this way, the von Kármán type nonlinearity ($I_1 = 1$, $I_2 = 0$) has linear terms in the strain-displacement relations for the transverse shear strains of the shell. That is, the only difference in Eqs. (8) between the VK and the MR approaches is that the latter has nonlinear terms in the transverse shear strains. The arguments described with Fig. 2 give an approach for the shell nonlinearity that is based more on a physical justification vs strictly an order-of-magnitude point of view. The effect of the additional nonlinearity is apparent for thicker, unsymmetrically laminated shell geometries, as will be seen in Sec. V.

C. Strain Displacement

The Reddy–Levinson–Murthy [13–15] shell kinematics of Eq. (10) have cubic functions of the transverse shell coordinate ζ for the in-plane displacements and assume the transverse displacement does not vary through the shell thickness. The linear components of the transverse shear stress (and, therefore, the transverse strains) vanish on the top and bottom surfaces of the shell. Reddy and Liu [13] develop these kinematics using a modified Sanders approach.

$$u_1(\xi_1, \xi_2, \zeta) = u\left(1 - \tfrac{\zeta}{R_1}\right) + \zeta\psi_1 + \zeta^3 k\left(\psi_1 + \tfrac{w_{,1}}{\alpha_1}\right)$$
$$u_2(\xi_1, \xi_2, \zeta) = v\left(1 - \tfrac{\zeta}{R_2}\right) + \zeta\psi_2 + \zeta^3 k\left(\psi_2 + \tfrac{w_{,2}}{\alpha_2}\right) \tag{10}$$
$$u_3(\xi_1, \xi_2) = w$$

where $k = -4/3h^2$; the five degrees of freedom u, v, w, ψ_1, and ψ_2 are functions of the shell middle plane coordinates ξ_1 and ξ_2; and a comma following a variable (e.g., $w_{,\gamma}$) refers to differentiation with respect to ξ_1 or ξ_2.

The linear components of the transverse shear strain are parabolic through the shell thickness, as given in Eq. (11).

$$e_{13} = \frac{1}{1 - \zeta/R_1}\left[\left(\psi_1 + \frac{w_{,1}}{\alpha_1}\right)(1 + 3\zeta^2 k)\right]$$
$$e_{23} = \frac{1}{1 - \zeta/R_2}\left[\left(\psi_2 + \frac{w_{,2}}{\alpha_2}\right)(1 + 3\zeta^2 k)\right] \tag{11}$$

Conversion to Cartesian coordinates is achieved using Eq. (12), in which the curvilinear coordinates ξ_1, ξ_2, and ζ are related to the Cartesian x, s, and z.

$$\alpha_1\,\mathrm{d}\xi_1 = \mathrm{d}x, \qquad \alpha_2\,\mathrm{d}\xi_2 = \mathrm{d}s, \qquad \mathrm{d}\zeta = \mathrm{d}z, \qquad (\cdot)_{,1} = \alpha_1(\cdot)_{,x}$$
$$(\cdot)_{,2} = \alpha_2(\cdot)_{,s} \tag{12}$$

Using the defined shell geometry and Eqs. (5), the remaining components of Green's strain-displacement relations are developed. The strain terms of Eqs. (13–15) follow from Eqs. (8), (10), and (11), applying the thin-shell assumption and then converting to Cartesian coordinates. The linear components of the strain are shown in Eqs. (13) and the nonlinear components in Eq. (14). The MR approach that retains terms of the order of θ^3 ($I_1 = 1$, $I_2 = 1$) includes all of the terms of Eqs. (13–15). The VK-type approach results by neglecting the nonlinear terms of Eqs. (15).

Linear strain terms are shown in Eq. (13).

$$e_1 = e_{11} = e_1^\circ + zk_{11} + z^3k_{13}, \qquad e_2 = e_{22} = e_2^\circ + zk_{21} + z^3k_{23}$$
$$e_6 = e_{12} = e_6^\circ + zk_{61} + z^3k_{63}, \qquad e_4 = e_{23} = e_4^\circ + z^2k_{42}$$
$$e_5 = e_{13} = e_5^\circ + z^2k_{52} \tag{13}$$

where

$$e_1^\circ = u_{,x} - \tfrac{w}{R_1}, \qquad e_2^\circ = v_{,s} - \tfrac{w}{R_2}, \qquad e_6^\circ = u_{,s} + v_{,x}$$
$$e_4^\circ = \psi_2 + w_{,s}, \qquad e_5^\circ = \psi_1 + w_{,x}, \qquad k_{11} = \psi_{1,x}$$
$$k_{13} = k(\psi_{1,x} + w_{,xx}), \qquad k_{21} = \psi_{2,s}, \qquad k_{23} = k(\psi_{2,s} + w_{,ss})$$
$$k_{42} = 3k(\psi_2 + w_{,s}), \qquad k_{52} = 3k(\psi_1 + w_{,x})$$
$$k_{61} = \psi_{1,s} + \psi_{2,x}, \qquad k_{63} = k(\psi_{1,s} + \psi_{2,x} + 2w_{,xs})$$

Nonlinear in-plane strain terms are given in Eqs. (14). These terms are the I_1 nonlinear terms.

$$E_i = E_i^\circ + z^r K_{ir} \qquad i = 1, 2, 6 \qquad r = 1, 2, 3, 4, 6$$
(implied summation on r)

where

$$E_1^\circ = \frac{1}{2} w_{,x}^2 + \frac{u w_{,x}}{R_1} + \frac{1}{2}\frac{u^2}{R_1^2}, \qquad K_{11} = \frac{\psi_1 w_{,x}}{R_1} + \frac{u\psi_1}{R_1^2}$$
$$K_{12} = \frac{1}{2}\frac{\psi_1^2}{R_1^2}, \qquad K_{13} = \frac{w_{,x}\psi_1 k}{R_1} + \frac{w_{,x}^2 k}{R_1} + \frac{u\psi_1 k}{R_1^2} + \frac{u w_{,x} k}{R_1^2}$$
$$K_{14} = \frac{\psi_1^2 k}{R_1^2} + \frac{\psi_1 w_{,x} k}{R_1^2}, \qquad K_{16} = \frac{1}{2}\frac{\psi_1^2 k^2}{R_1^2} + \frac{\psi_1 w_{,x} k^2}{R_1^2} + \frac{1}{2}\frac{w_{,x}^2 k^2}{R_1^2} \tag{14a}$$

$$E_2^\circ = \frac{1}{2} w_{,s}^2 + \frac{v w_{,s}}{R_2} + \frac{1}{2}\frac{v^2}{R_2^2}, \qquad K_{21} = \frac{\psi_2 w_{,s}}{R_2} + \frac{\psi_2 v}{R_2^2}$$
$$K_{22} = \frac{1}{2}\frac{\psi_2^2}{R_2^2}, \qquad K_{23} = \frac{w_{,s}\psi_2 k}{R_2} + \frac{w_{,s}^2 k}{R_2} + \frac{v\psi_2 k}{R_2^2} + \frac{v w_{,s} k}{R_2^2}$$
$$K_{24} = \frac{\psi_2^2 k}{R_2^2} + \frac{\psi_2 w_{,s} k}{R_2^2}, \qquad K_{26} = \frac{1}{2}\frac{\psi_2^2 k^2}{R_2^2} + \frac{\psi_2 w_{,s} k^2}{R_2^2} + \frac{1}{2}\frac{w_{,s}^2 k^2}{R_2^2} \tag{14b}$$

$$E_6^\circ = w_{,x} w_{,s} + \frac{u w_{,s}}{R_1} + \frac{v w_{,x}}{R_2} + \frac{uv}{R_1 R_2}$$
$$K_{61} = \frac{\psi_1 w_{,s}}{R_1} + \frac{\psi_2 w_{,x}}{R_2} + \frac{\psi_2 u}{R_1 R_2} + \frac{\psi_1 v}{R_1 R_2}, \qquad K_{62} = \frac{\psi_1 \psi_2}{R_1 R_2}$$
$$K_{63} = \frac{w_{,s}\psi_1 k}{R_1} + w_{,x} w_{,s} k\left(\frac{1}{R_1} + \frac{1}{R_2}\right) + \frac{w_{,x}\psi_2 k}{R_2} + \frac{uk}{R_1 R_2}(\psi_2 + w_{,s}) + \frac{vk}{R_1 R_2}(\psi_1 + w_{,x})$$
$$K_{64} = \frac{k}{R_1 R_2}(w_{,x}\psi_2 + w_{,s}\psi_1 + 2\psi_1\psi_2)$$
$$K_{66} = \frac{k^2}{R_1 R_2}(\psi_1\psi_2 + w_{,x}\psi_2 + w_{,s}\psi_1 + w_{,x} w_{,s}) \tag{14c}$$

Nonlinear transverse strain terms are given in Eqs. (15). These terms are the I_2 nonlinear terms.

$$E_m = E_m^\circ + z^t K_{mt} \qquad m = 4, 5 \qquad t = 1, 2, 3, 5$$
(implied summation on t) (15)

$$E_5^\circ = u_{,x}\psi_1 + v_{,x}\psi_2 - \tfrac{\psi_1 w}{R_1}, \qquad K_{51} = \psi_1\psi_{1,x} + \psi_2\psi_{2,x}$$
$$K_{52} = 3k[u_{,x}(\psi_1 + w_{,x}) + v_{,x}(\psi_2 + w_{,s}) - \tfrac{w}{R_1}(\psi_1 + w_{,x})]$$
$$K_{53} = k(w_{,xx}\psi_1 + 4\psi_1\psi_{1,x} + w_{,xs}\psi_2 + 4\psi_2\psi_{2,x} + 3w_{,x}\psi_{1,x} + 3w_{,s}\psi_{2,x})$$
$$K_{55} = 3k^2[w_{,xx}\psi_1 + \psi_1\psi_{1,x} + w_{,xs}\psi_2 + \psi_2\psi_{2,x} + w_{,x}(w_{,xx} + \psi_{1,x}) + w_{,s}(w_{,xs} + \psi_{2,x})] \tag{15a}$$

$$E_4^\circ = u_{,s}\psi_1 + v_{,s}\psi_2 - \tfrac{\psi_2 w}{R_2}, \qquad K_{41} = \psi_1\psi_{1,s} + \psi_2\psi_{2,s}$$
$$K_{42} = 3k[u_{,s}(\psi_1 + w_{,x}) + v_{,s}(\psi_2 + w_{,s}) - \tfrac{w}{R_2}(\psi_2 + w_{,s})]$$
$$K_{43} = k(w_{,xs}\psi_1 + 4\psi_1\psi_{1,s} + w_{,ss}\psi_2 + 4\psi_2\psi_{2,s} + 3w_{,x}\psi_{1,s} + 3w_{,s}\psi_{2,s})$$
$$K_{45} = 3k^2[w_{,xs}\psi_1 + \psi_1\psi_{1,s} + w_{,ss}\psi_2 + \psi_2\psi_{2,s} + w_{,x}(w_{,xs} + \psi_{1,s}) + w_{,s}(w_{,ss} + \psi_{2,s})] \tag{15b}$$

The transverse normal strain of Eq. (9) is not given, as the plane stress assumption ($\sigma_{33} = 0$) in the following section will eliminate it.

D. Shell Potential Energy

Consider thin-shell geometries in which the transverse normal stress is assumed to be approximately zero. Following Reddy and Liu [13] arguments, the magnitude of the transverse normal stress is of the order of h/R and, away from a shell boundary, the transverse shear stresses are of the order of h/L. (From Fig. 1, h is the shell thickness, R is a radius of curvature, and L is the shell length $2a$ or $2b$). Therefore, we can consider the transverse normal stress to be small compared with the transverse shear stresses when $R \gg L$. As mentioned, setting the transverse normal stress to zero in the constitutive relations allows the transverse normal strain to be eliminated.

Consequently, assume an orthotropic material, such that in material axes (i.e., axes aligned with the fiber direction and perpendicular to the fiber direction)

$$\begin{Bmatrix} \sigma_1 \\ \sigma_2 \\ \sigma_3 \\ \sigma_4 \\ \sigma_5 \end{Bmatrix} = \begin{bmatrix} Q_{11} & Q_{12} & 0 & 0 & 0 \\ Q_{12} & Q_{22} & 0 & 0 & 0 \\ 0 & 0 & Q_{66} & 0 & 0 \\ 0 & 0 & 0 & Q_{44} & 0 \\ 0 & 0 & 0 & 0 & Q_{55} \end{bmatrix} \begin{Bmatrix} \varepsilon_1 \\ \varepsilon_2 \\ \varepsilon_3 \\ \varepsilon_4 \\ \varepsilon_5 \end{Bmatrix} \tag{16}$$

where the reduced stiffnesses Q_{ij} are defined as follows and E_α, $\upsilon_{\alpha\beta}$, and G_{ij} are engineering properties.

$$Q_{11} = \tfrac{E_1}{\Delta}, \qquad Q_{22} = \tfrac{E_2}{\Delta}, \qquad Q_{12} = \upsilon_{12}\tfrac{E_2}{\Delta}, \qquad Q_{66} = G_{12}$$
$$Q_{44} = G_{23}, \qquad Q_{55} = G_{13}, \qquad \Delta = 1 - \upsilon_{21}\upsilon_{12}$$

and shorthand notation for the stress components (and, similarly, for the strains) is defined as

$$\sigma_1 = \sigma_{11}, \qquad \sigma_2 = \sigma_{22}, \qquad \sigma_6 = \sigma_{12}, \qquad \sigma_4 = \sigma_{23}$$
$$\sigma_5 = \sigma_{13}$$

Eq. (16) is transformed to shell axes, giving for ply n

$$\begin{Bmatrix}\sigma_1\\ \sigma_2\\ \sigma_6\end{Bmatrix}^n = \begin{bmatrix}\bar{Q}_{11} & \bar{Q}_{12} & \bar{Q}_{16}\\ & \bar{Q}_{22} & \bar{Q}_{26}\\ & & \bar{Q}_{66}\end{bmatrix}^n \begin{Bmatrix}\varepsilon_1\\ \varepsilon_2\\ \varepsilon_6\end{Bmatrix}$$
$$\begin{Bmatrix}\sigma_4\\ \sigma_5\end{Bmatrix}^n = \begin{bmatrix}\bar{Q}_{44} & \bar{Q}_{45}\\ & \bar{Q}_{55}\end{bmatrix}^n \begin{Bmatrix}\varepsilon_4\\ \varepsilon_5\end{Bmatrix} \tag{17}$$

where the $\bar{Q}_{ij}$ are elements of the symmetric transformed reduced-stiffness matrices and are a function of the angle between the shell x axis and the fiber direction of ply n (see, for example, Jones [27]).

A displacement-based finite element solution results by minimizing the total potential energy of the shell to get equilibrium. The total potential energy is the sum of the strain energy and the potential of the external loading.

$$\pi_p = U + V \tag{18}$$

where

$$U = \frac{1}{2}\int_\Omega \int_h (\sigma_1\varepsilon_1 + \sigma_2\varepsilon_2 + \sigma_3\varepsilon_3 + \sigma_4\varepsilon_4 + \sigma_5\varepsilon_5)\,\mathrm{dVol}$$
$$V = \int_\Gamma \bar{N}\,\bar{u}\,\mathrm{d}\xi$$
$$\mathrm{dVol} = \alpha_1\alpha_2\left(1 - \frac{\zeta}{R_1}\right)\left(1 - \frac{\zeta}{R_2}\right)\mathrm{d}\xi_1\,\mathrm{d}\xi_2\,\mathrm{d}\zeta \cong \mathrm{d}x\,\mathrm{d}s\,\mathrm{d}z$$

where $\bar{N}$ is the in-plane loading perpendicular to the shell boundary Γ, compression is positive, and $\bar{u}$ is the in-plane displacement of the boundary normal to the boundary.

Using Eq. (17), the shell strain energy can be written using indicial notation (with implied summation on repeated indices) for subsequent ease in manipulation, as shown in Eq. (19). The strains are separated into linear e_i and nonlinear E_i parts in the second half of Eq. (19) [see also Eqs. (13–15)].

$$U = \frac{1}{2}\int_\Omega \int_h (\bar{Q}_{ij}\varepsilon_i\varepsilon_j + \bar{Q}_{mn}\varepsilon_m\varepsilon_n)\,\mathrm{d}z\,\mathrm{d}x\,\mathrm{d}s = \frac{1}{2}\int_\Omega \int_h [\bar{Q}_{ij}(e_i + E_i)(e_j + E_j) + \bar{Q}_{mn}(e_m + E_m)(e_n + E_m)]\,\mathrm{d}z\,\mathrm{d}x\,\mathrm{d}s \tag{19}$$

where $i, j = 1, 2, 6$ and $m, n = 4, 5$.

Expanding the second half of Eq. (19) leads to the form of the strain energy in Eq. (20) that will be convenient for subsequent programming.

$$U = U_K + U_{N_1} + U_{N_2} \tag{20}$$

where

$$U_K = \frac{1}{2}\int_\Omega \int_h (\bar{Q}_{ij}e_ie_j + \bar{Q}_{mn}e_me_n)\,\mathrm{d}V$$
$$U_{N_1} = \frac{1}{2}\int_\Omega \int_h 2(\bar{Q}_{ij}e_iE_j + \bar{Q}_{mn}e_mE_n)\,\mathrm{d}V$$
$$U_{N_2} = \frac{1}{2}\int_\Omega \int_h (\bar{Q}_{ij}E_iE_j + \bar{Q}_{mn}E_mE_n)\,\mathrm{d}V$$

Upon integrating through the shell thickness,

$$U_K = \tfrac{1}{2}\Big[e_i^\circ e_i^\circ A_{ij} + 2e_i^\circ(k_{j1}B_{ij} + k_{j3}E_{ij}) + k_{i1}k_{j1}D_{ij} + 2k_{i1}k_{j3}F_{ij} + k_{i3}k_{j3}H_{ij} + e_m^\circ e_n^\circ A_{mn} + 2e_m^\circ k_{n2}D_{mn} + k_{m2}k_{n2}F_{mn}\Big]\,\mathrm{d}x\,\mathrm{d}s \tag{21}$$

$$U_{N_1} = \frac{1}{2}\int_\Omega 2\Big[e_i^\circ E_j^\circ A_{ij} + e_i^\circ(K_{j1}B_{ij} + K_{j2}D_{ij} + K_{j3}E_{ij} + K_{j4}F_{ij} + K_{j6}H_{ij}) + E_j^\circ(k_{i1}B_{ij} + k_{i3}E_{ij}) + k_{i1}K_{j1}D_{ij} + k_{i1}K_{j2}E_{ij} + (k_{i1}K_{j3} + k_{i3}K_{j1})F_{ij} + (k_{i1}K_{j4} + k_{i3}K_{j2})G_{ij} + k_{i3}K_{j3}H_{ij} + (k_{i1}K_{j6} + k_{i3}K_{j4})I_{ij} + k_{i3}K_{j6}P_{ij}\Big]\,\mathrm{d}x\,\mathrm{d}s + \frac{1}{2}\int_\Omega 2\Big[e_m^\circ E_n^\circ A_{mn} + e_m^\circ(K_{n1}B_{mn} + K_{n2}D_{mn} + K_{n3}E_{mn} + K_{n5}G_{mn}) + E_n^\circ k_{m2}D_{mn} + k_{m2}k_{n1}E_{mn} + k_{m2}K_{n2}F_{mn} + k_{m2}K_{n3}G_{mn} + k_{m2}K_{n5}I_{mn}\Big]\,\mathrm{d}x\,\mathrm{d}s \tag{22}$$

$$U_{N_2} = \frac{1}{2}\int_\Omega [E_i^\circ E_i^\circ A_{ij} + 2E_i^\circ K_{j1}B_{ij} + D_{ij}(2E_i^\circ K_{j2} + K_{i1}K_{j1}) + E_{ij}(2E_i^\circ K_{j3} + 2K_{i1}K_{j2}) + F_{ij}(2E_i^\circ K_{j4} + 2K_{i1}K_{j3} + K_{i2}K_{j2}) + G_{ij}(2K_{i1}K_{j4} + 2K_{i2}K_{j3}) + H_{ij}(2E_i^\circ K_{j6} + 2K_{i2}K_{j4} + K_{i3}K_{j3}) + I_{ij}(2K_{i1}K_{j6} + 2K_{i3}K_{j4}) + J_{ij}(2K_{i2}K_{j6} + K_{i4}K_{j4}) + 2P_{ij}K_{i3}K_{j6} + 2R_{ij}K_{i4}K_{j6} + T_{ij}K_{i6}K_{j6}]\,\mathrm{d}x\,\mathrm{d}s + \frac{1}{2}\int_\Omega [E_m^\circ E_n^\circ A_{mn} + 2E_m^\circ K_{n1}B_{mn} + D_{mn}(2E_m^\circ K_{n2} + K_{m1}K_{n1}) + E_{mn}(2E_m^\circ K_{n3} + 2K_{m1}K_{n2}) + F_{mn}(2K_{m1}K_{n3} + K_{m2}K_{n2}) + G_{mn}(2E_m^\circ K_{n5} + 2K_{m2}K_{n3}) + H_{mn}(2K_{m1}K_{n5} + K_{m3}K_{n3}) + 2K_{m2}K_{n5}I_{mn} + 2K_{m3}K_{n5}J_{mn} + \mathrm{K}_{m5}K_{n5}R_{mn}]\,\mathrm{d}x\,\mathrm{d}s \tag{23}$$

where the elasticity arrays are defined in Eqs. (24), and terms with indices i and j are contributions from the in-plane strains and terms with indices m and n are from the transverse strains.

$$[A_{ij}, B_{ij}, D_{ij}, E_{ij}, F_{ij}, G_{ij}, H_{ij}, I_{ij}, J_{ij}, P_{ij}, R_{ij}, T_{ij}] = \int_h \bar{Q}_{ij}[1, z, z^2, z^3, z^4, z^5, z^6, z^7, z^8, z^9, z^{10}, z^{12}]\,\mathrm{d}z$$
$$[A_{mn}, B_{mn}, D_{mn}, E_{mn}, F_{mn}, G_{mn}, H_{mn}, I_{mn}, J_{mn}, R_{mn}] = \int_h \bar{Q}_{mn}[1, z, z^2, z^3, z^4, z^5, z^6, z^7, z^8, z^{10}]\,\mathrm{d}z \tag{24}$$

The strain energy term U_K [Eq. (21)] will give constant stiffness terms. The energy term U_{N_1} [Eq. (22)] will result in stiffness terms that are linear in displacement. The energy term U_{N_2} [Eq. (23)] will give stiffness terms that are quadratic in displacement.

III. Numerical Solution

The potential energy of the shell presented in the previous section is approximated using a mesh of 36-degree-of-freedom curved shell elements. Each of the corner nodes has seven DOF and midside nodes have two DOF. Hermitian interpolation is used for the transverse displacement w and its two derivatives $w_{,x}$ and $w_{,s}$, based on element corner nodes for these DOF. In addition, each corner node has bending DOF, ψ_1 and ψ_2, and these are interpolated with Lagrangian functions. Finally, the in-plane displacements u and v are interpolated with quadratic Lagrangian functions, based on corner-node DOF and midside-node DOF.

The elemental potential energy of the discretized domain is given in Eq. (25), where q is a column array of elemental degrees of freedom. The stiffness arrays K, N_1, and N_2 are defined in such a way so that subsequent derivatives yield repeating forms; see similar developments in Palazotto and Dennis [28].

$$\pi_p = \frac{q^T}{2}\left(K + \frac{N_1}{3} + \frac{N_2}{6}\right)q - q^T R \tag{25}$$

Equilibrium follows from the first variation of the total potential energy.

$$\delta\pi_p = \delta q^T\left[\left(K + \frac{N_1}{2} + \frac{N_2}{3}\right)q - R\right] = 0$$
$$\left(K + \frac{N_1}{2} + \frac{N_2}{3}\right)q - R = 0 \equiv F(q) = 0 \tag{26}$$

An incremental/iterative Newton–Raphson solution results after expanding the equilibrium equations of Eq. (26) into a truncated Taylor's series [see Eq. (27)].

$$F(q + \Delta q) = F(q) + \frac{\partial F}{\partial q}\Delta q + \ldots = 0 \qquad \frac{\partial F}{\partial q}\Delta q = -F(q)$$
$$(K + N_1 + N_2)\Delta q = -F(q), \qquad K_T\Delta q = -F(q) \tag{27}$$

For a given load or displacement increment, iteration of the final expression of Eq. (27) continues until the change of a norm of displacements is less than 1%, signifying that equilibrium has been satisfied.

Equation (27) was coded into Fortran 90, in which Mathematica performed the many symbolic matrix multiplications that resulted in Fortran subroutines. Solution times can be significantly shortened by exploiting parallelism. Two simple message passing interface (MPI) implementations were used to parallelize the calculation of the elemental stiffnesses and assembly into the global stiffness matrix and to solve the resulting large system of simultaneous equations. A straightforward implementation of the worker–manager model allows the workers to calculate the elemental stiffnesses, and the manager receives the calculations and assembles into the global stiffness matrix [29]. A simple Gaussian elimination solution algorithm was used. In the parallel algorithm, the global stiffness is stored interleaved so that work is better distributed to the workers. Each worker then, in parallel, eliminates its own rows [30].

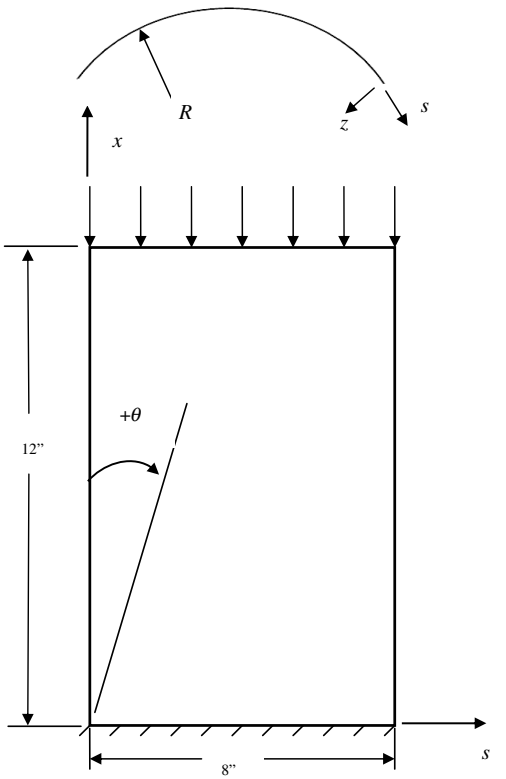

Fig. 3 Geometry of Wilkins [22,23] cylindrical panels. The load is input via a uniform prescribed axial displacement along $x = 12''$ (0.305 m). $R = 12''$ for all panels. CCSS boundary condition, top: all DOF are fixed, except u is prescribed; bottom: all DOF are fixed; vertical edges: only w and ψ_1 are fixed. CCSS boundary condition, top: all DOF are fixed, except u is prescribed; bottom: all DOF are fixed; vertical edges: only u and v are fixed.

Table 1 Four laminates examined for nonlinear response

Laminate	Panel thickness h, in.	Boundary conditions	Wilkins no. ([22–24])
$[0/90]_s$	0.0289 (0.734 mm)	CCSS	21A
$[0]_{6s}$	0.1039 (2.64 mm)	CCCC, CCSS	47B
$[\pm 45]_{2s}$	0.598 (1.52 mm)	CCCC	19E
$[-30]_{2s}$	0.0282 (0.716 mm)	CCSS	37A

All numerical simulations were run on the Aeronautical Systems Center Major Shared Resource Center SGI Origin 3900. The SGI Origin 3900 is a shared memory system with 4 nodes of 512 CPUs each. Each CPU is a 700 MHz R14000 MIPS processor and has a 32 KB primary data cache, a 32 KB primary instruction cache, and an 8 MB onboard cache [31]. Most of the solutions were based on 8 or 16 processors. Hardware limitations, due to the size of some problems and the algorithms used, resulted in significant speedups compared with using either one or two processors.

Extensive verification of the approach and algorithms was performed. Doubly curved, unsymmetrically laminated shells, under various loadings, were simulated for both linear and nonlinear responses and compare favorably with the published results of, for example, Reddy and Liu [13] and Reddy et al. [32].

IV. Thin, Symmetrically Laminated Cylindrical Panels

Comparisons to existing experimental results represent a more challenging verification of the present numerical approach. The VK-type nonlinearity [$I_1 = 1, I_2 = 0$, see Eqs. (8), (13), and (14)] and the MR nonlinearity [$I_1 = 1$, $I_2 = 1$, see Eqs. (8) and (13–15)] are applied to axially compressed, symmetrically laminated cylindrical shell panels. Comparisons are made to selected geometries from the extensive experimental results of Wilkins [22,23] and Love and Brubaker [24]. The VK and MR approaches are expected to yield similar results, as all of the Wilkins panels are thin ($L/h > 80$, where L is the length of a side of the panel and h is the panel thickness) and symmetrically laminated. Thicker, unsymmetrically stacked laminates are examined in the next section and the influence of the additional nonlinear terms in the MR approach is evident.

The results of Wilkins [22,23] and Love and Brubaker [24] were chosen for comparisons for several reasons. The testing done by

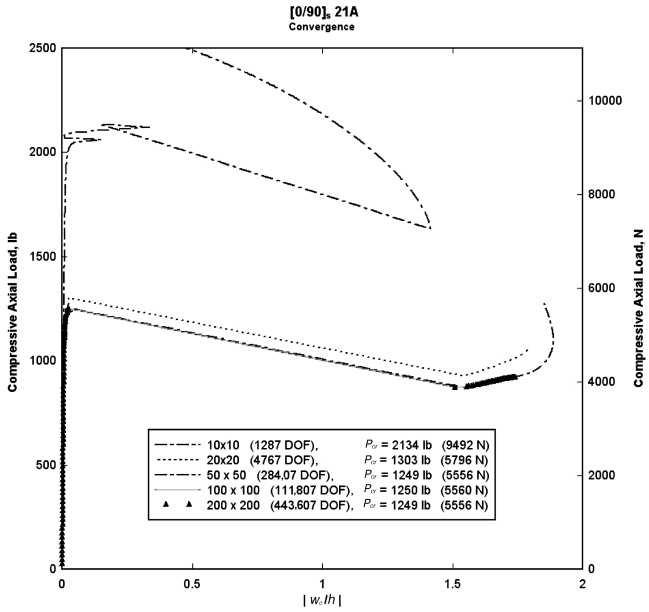

Fig. 4 Convergence of middle panel deflection for cross-ply laminate $[0/90]_s$, Wilkins panel 21A. The number of degrees of freedom are given for each mesh.

Wilkins was extensive; many laminate orientations and thicknesses were tested and their results appear to have been repeatable. Because of the scope of the Wilkins study, the present approach is applied to four different types of symmetrically stacked laminates. In addition, the researchers report buckling loads based on two experimental indications, described next. Furthermore, they document full-field panel buckling shapes from moiré fringe photographs. Finally, the researchers report analytical results, based on a classical buckling approach, that are significantly different from the experimental results. Hence, improvements in predicted results were anticipated with the present numerical approach.

The cylindrical panels are 12 in. (0.305 m) in length in the flat direction (along the x axis) and 8 in. (0.203 m) in length circumferentially (s axis), as shown in Fig. 3, in which the radius of curvature for all panels is 12 in. Wilkins [22,23] assumed the orthotropic material properties shown in Eq. (28) for the ply fiber (direction 1) and the matrix (direction 2) directions. Properties for directions 1–3 were not reported and those shown in Eq. (28) were used for the present analytical approach.

$$E_1 = 20 \times 10^6 \text{ psi} = 138 \text{ GPa}$$
$$E_2 = 2.1 \times 10^6 \text{ psi} = 14.5 \text{ GPa}$$
$$G_{12} = 0.85 \times 10^6 \text{ psi} = 5.9 \text{ GPa}, \qquad \nu_{12} = 0.21 \tag{28}$$
$$G_{13} = 0.85 \times 10^6 \text{ psi} = 5.9 \text{ GPa}$$
$$G_{23} = 0.425 \times 10^6 \text{ psi} = 2.9 \text{ GPa}$$

All panels are clamped at the top and bottom edges (at $x = 0$, 12 in.) and the load is input by prescribing the axial displacement u along the top edge in the negative x direction. Wilkins [22,23] attempted two sets of boundary conditions for the vertical (unloaded) edges. Boundary condition CCSS included the aforementioned clamped conditions at the top and bottom of the panel and simple supports for the vertical edges. Only the transverse displacement w and the bending rotation ψ_1 (rotation about s axis) are prescribed

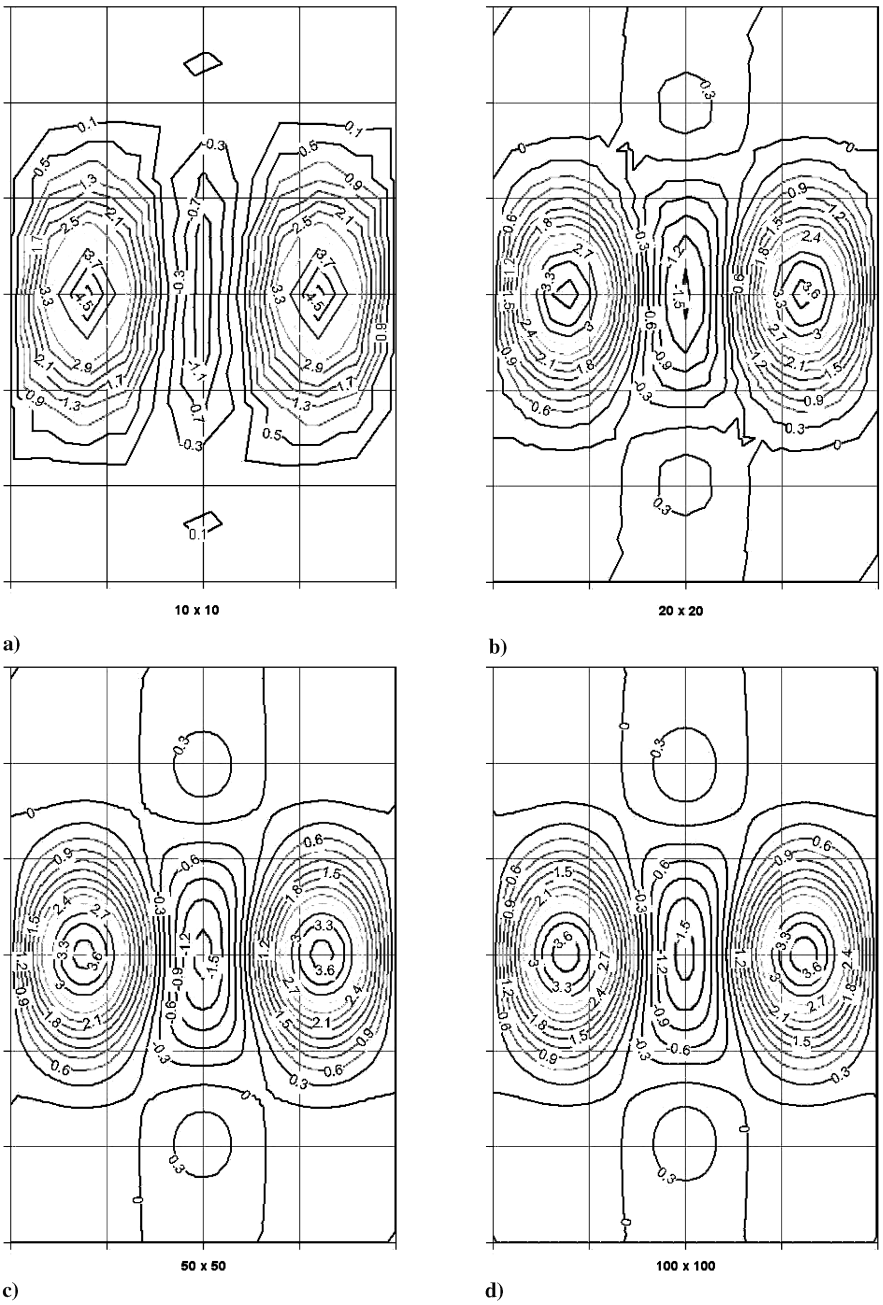

Fig. 5 Postbuckle contours of constant shell panel deflection w/h for axial compression (w_c/h about 1.5 in Fig. 4), $[0/90]_s$, panel 21A. Contour plots developed using DPlot (www.dplot.com/).

along the vertical edges. In-plane displacements u and v along the vertical edges were assumed to be free, based on experimental descriptions given by Love and Brubaker[24]. Boundary condition CCCC has clamped conditions for all shell panel boundaries.

Four laminates were numerically compressed and their nonlinear responses traced and compared with experimental results from Wilkins, Brubaker, and Love[22–24]. Table 1 gives the specific cases. Convergence of the numerical solution is initially presented using the first laminate in the table. A brief discussion comparing the numerical simulation and experimental behavior of each of the panels given in the table follows.

A. Convergence

Regular meshes of 10, 20, 50, 100, and 200 elements along both the x and s directions were simulated to determine convergence requirements. The cross-ply panel $[0/90]_s$ (Wilkins panel 21A) was studied for convergence. Figure 4 shows the center panel deflection normalized by the panel thickness vs the total axial load P. The panel experiences little deflection with increasing axial compression until reaching a critical load, when it suddenly buckles. The buckled panel has experienced significant deflections. Figure 4 shows that the three most refined meshes give a consistent shell response. The converged numerical critical load is approximately 1250 lb (5560 N).

A numerical imperfection is not required in the present formulation to trigger the limit point buckling seen in Fig. 4. However, as discussed in Wardle [33], the solution algorithm may skip lower energy bifurcation deformation modes. That is, the actual panels may experience bifurcation at a load less than the limit point load predicted in the present formulation. As discussed in Wardle, the addition of numerical imperfections is a technique that allows a bifurcation solution if one is present.

Full-field convergence is also examined by plotting contours of constant deflection (see Fig. 5). The deflection contour plots for this panel geometry reveal three half-sine waves in the circumferential direction with significant deflection in the outer two waves (approximately 3.6 times the panel thickness). The contours of Fig. 5 reveal the center of the panel deflects negatively (i.e., away from the center of curvature). Larger deflections are experienced in the two outer half-sine waves and these regions of the panel deflect toward the center of curvature. The convergence study shows the 100×100 regular mesh gives appropriate results for both the critical load and the full-field deflections and, unless otherwise stated, remaining analyses are based on this mesh.

B. Comparison with Wilkins's Experimental Results

The numerical response of each of the four panels listed in Table 1 is compared with the experimental results of Wilkins[22,23]. The center panel deflection is plotted vs the total axial load based on the response of the 100×100 mesh. Wilkins determined the experimental buckling load by two methods, moiré and Southwell, and these two loads are superimposed on the present numerical response. The moiré fringe patterns helped Wilkins determine the onset of panel buckling. A master grading containing closely spaced parallel lines was placed in front of the panel specimen. Light directed obliquely onto and through the master grading left a shadow on the panel. As the panel deflected, fringes resulted due to interference between the master grading and the shadow. The fringes are a measure of the out-of-plane displacement w, and w is approximated by Eq. (29); see Dally and Riley [34]. The pitch p of the master grading that Wilkins used was probably 0.01 (100 lines/in.), although at least some of the panel tests used approximately 50 lines/in. As Eq. (29) shows, based on a pitch of 100 lines/in., each fringe in the panel photographs given by Wilkins represents about

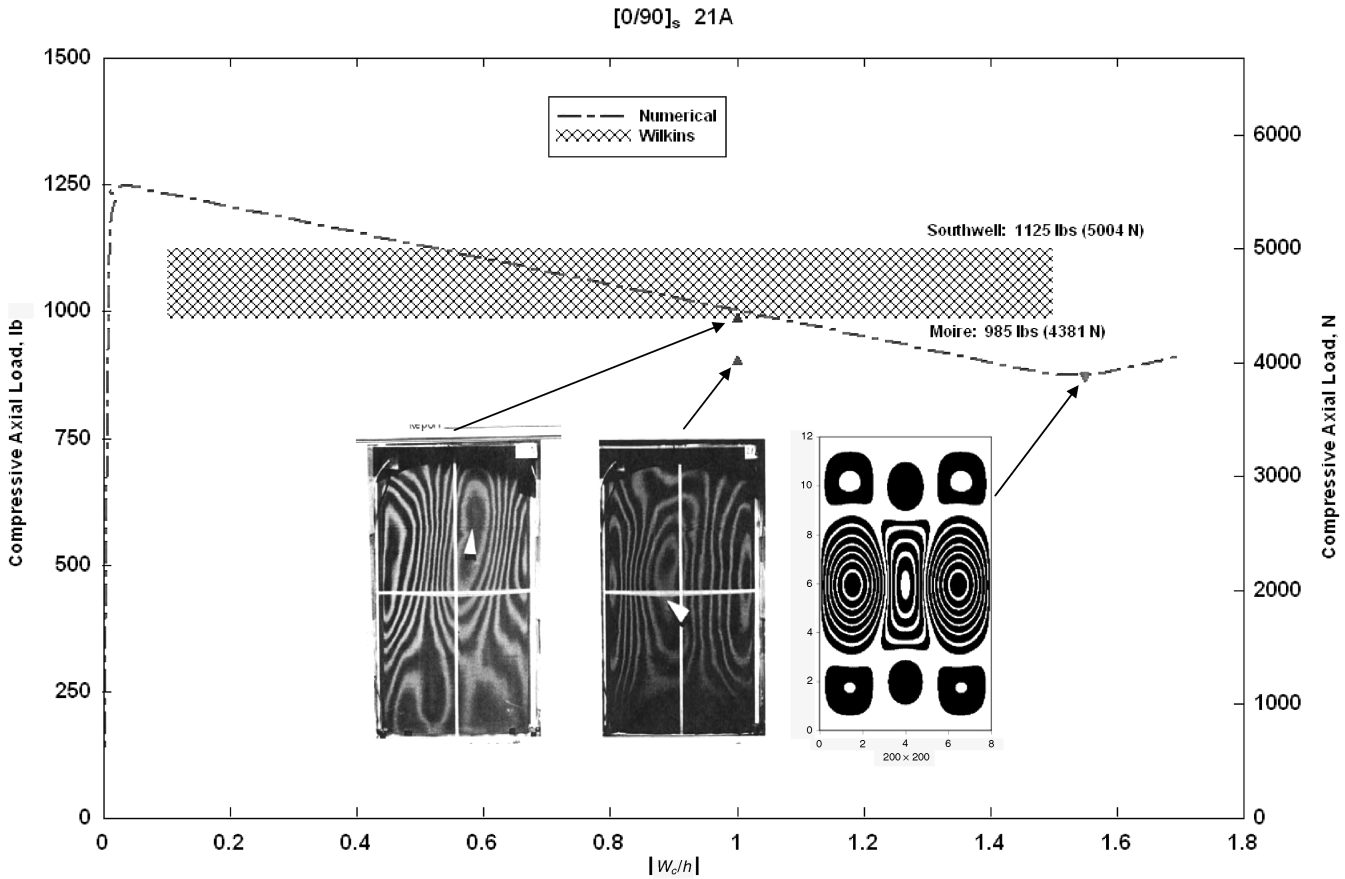

Fig. 6 Numerical center panel deflection vs axial load and Wilkins's experimental results. Moiré photographs for Wilkins panels 21A (left) and 21B (middle). Panel 21B has a slightly smaller thickness [$h = 0.0282$ in. (0.72 mm) vs 0.0289 for 21A]. Numerical contour plot from the 200 × 200 mesh and each fringe represents approximately 0.015 in. (0.38 mm) of deflection.

0.006 in. (0.15 mm) of displacement w. In Wilkins, the onset of buckling was assumed by watching for "rapid fringe movement and the decreasing distance between adjacent fringes."

$$w = \frac{np}{\tan\alpha} = \frac{0.01}{\tan 60\,\text{deg}} \cong 0.006\ \text{in.}\ (\approx 0.15\ \text{mm}) \quad (29)$$

displacement per fringe

where w is the panel out-of-plane displacement in inches; p is the pitch of the master grading, 0.01 in./line (100 lines/in.); α is the angle of the incident light, =60 deg; and n is the order or fringe.

Additionally, the Southwell method provides a buckling load based on load-deflection data and is described by Timoshenko and Gere [35]. Wilkins [22,23] concluded that the moiré and Southwell plot methods provide a lower and upper bound, respectively, for the critical panel load. Numerical simulation contours of constant panel deflection are compared with the moiré panel photographs taken by Wilkins near the maximum load.

1. $[0/90]_s$ *Wilkins Panel 21A*

The center panel deflection vs total axial load is plotted in Fig. 6 for the cross-ply laminate, $[0/90]_s$. This panel experiences sudden, relatively large center panel deflections at an axial load, P, equal to 1250 lb (5560 N). The numerical buckling load overpredicts the Wilkins [22,23] experimental loads of 1125 lb (5004 N, via Southwell plot method) and 985 lb (4381 N, from moiré fringe data). The numerical full-field panel response is characterized by three half-sine waves circumferentially and compares qualitatively well to the Wilkins moiré result. However, the Wilkins panel did not deflect as much as the numerical response. That is, the moiré data give a normalized center panel deflection of about one ($w_c/h = 1$), but the analytical panel deflects about 1.5 times the panel thickness. Furthermore, the outer half-sine waves deflect significantly more than that shown in the experimental moiré fringe pattern. That is, compare Fig. 5 to the Wilkins photograph of Fig. 6. The experimental results show some skewing in the deflection pattern that the numerical response does not (see Fig. 6 contours). Inevitably, boundary conditions in the actual panel experiments do not agree with the idealizations assumed in Fig. 3.

2. $[0]_{6s}$ *Wilkins Panel 47B*

The unidirectional laminate $[0]_{6s}$ (Wilkins panel 47B) does not buckle according to the numerical response. Instead, the panel center deflection shows a small gradual increase with axial compression until the total compressive load reaches approximately 20,000 lb (88,960 N). For loads increasing above 20,000 lb, the panel center response disproportionately increases. Figure 7 shows this response for both the CCCC and CCSS boundary conditions. The single half-sine wave in each direction compares well to the Wilkins [22,23] result. In addition, the magnitude of the full-field deflection compares well with approximately the same number of fringes shown in the figure (see also Fig. 8). Once again, some skewing is evident in the deflection pattern from the moiré photograph, perhaps due to inconsistencies in the actual panel boundary conditions.

This panel geometry was also loaded numerically using the MR nonlinearity and the response was very close to the VK response.

3. $[\pm 45]_{2s}$ *Wilkins Panel 19E*

Figure 9 shows the center panel deflection vs axial load for the angle-ply laminate $[\pm 45]_{2s}$. This panel deflects a significant amount

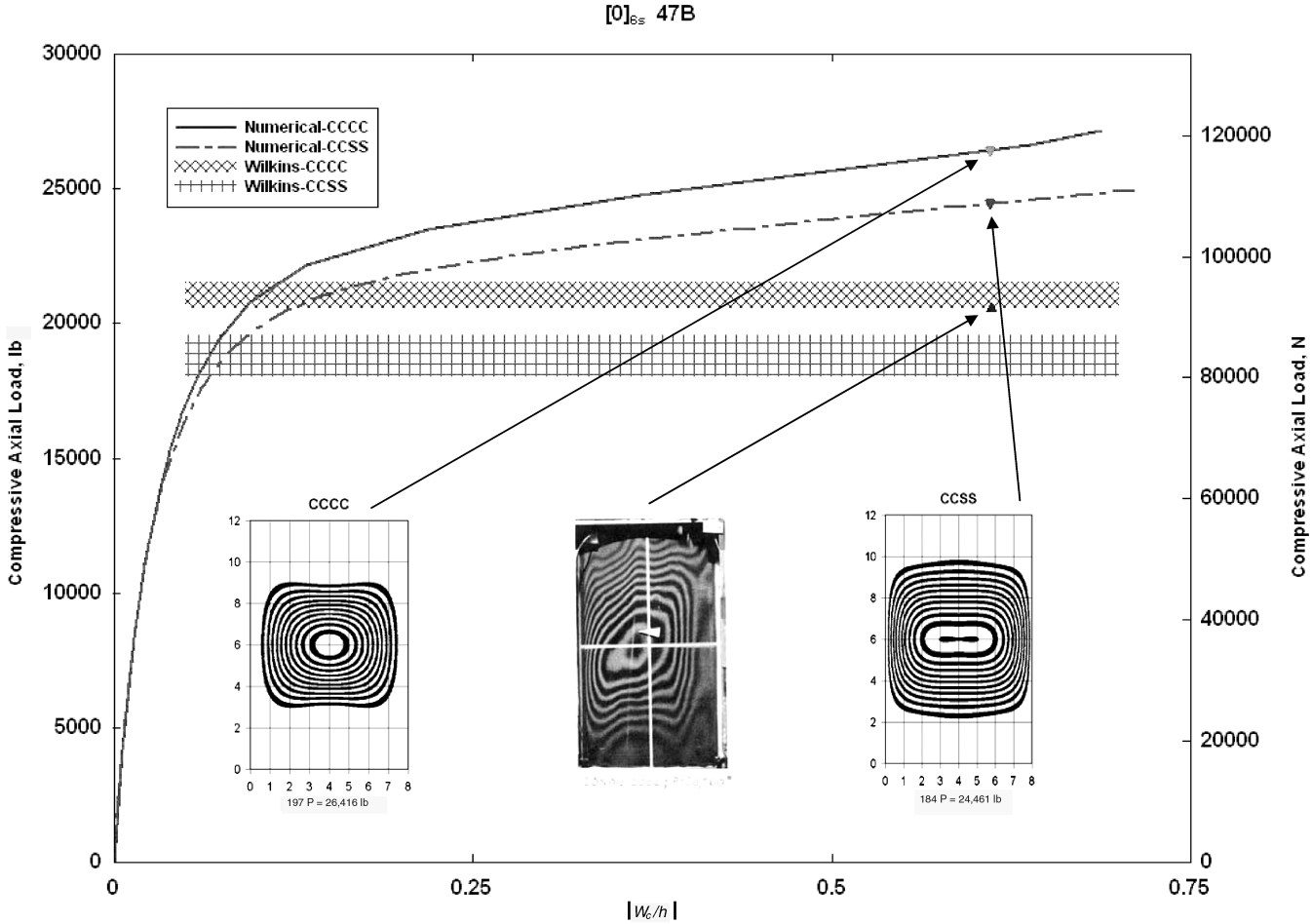

Fig. 7 Numerical center panel deflection vs axial load and Wilkins experimental results ($h = 0.1039$ in. $= 2.64$ mm). The Wilkins CCCC crosshatched region is bounded by 20,560 lb (91,450 N) and 21,538 lb (95,800 N). The CCSS crosshatched region is bounded by 18,000 lb (80,060 N) and 19,598 lb (87,170 N).

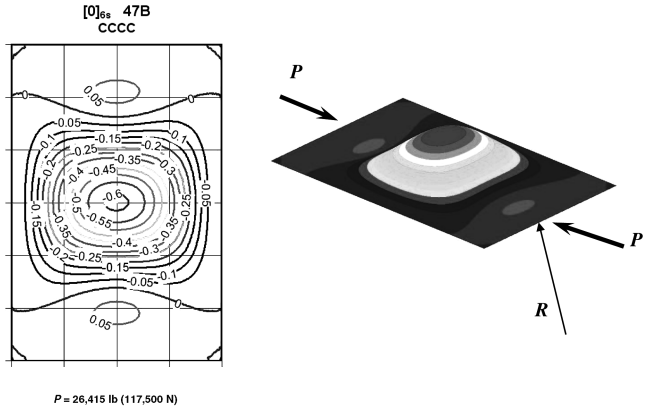

Fig. 8 Full-field panel deflection (w/h) for the unidirectional laminate $[0]_{6s}$. Center panel deflects outward, i.e., away from the panel center of curvature.

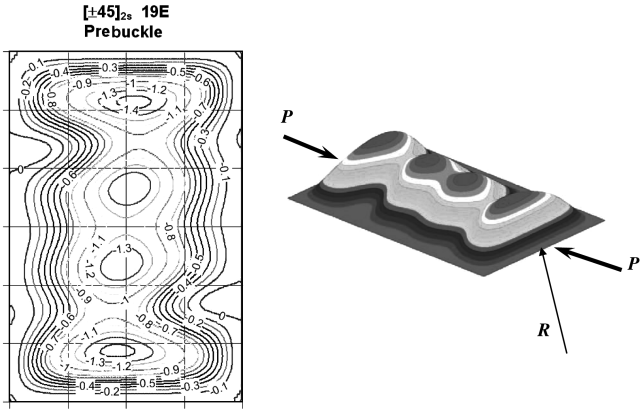

Fig. 10 Prebuckled contours for the angle-ply laminate $[\pm 45]_{2s}$.

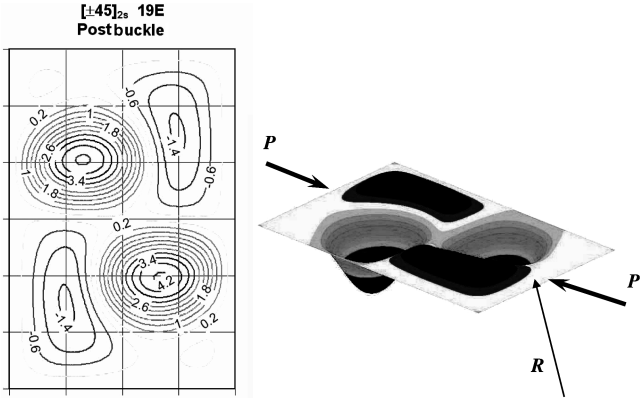

Fig. 11 Postbuckled contours for the angle-ply laminate $[\pm 45]_{2s}$.

before buckling. In addition, although the center panel deflection is already greater than the thickness of the panel before the critical load, the postbuckle shows deflection in the opposite direction, i.e., toward the center of curvature. That is, the center panel deflection reverses itself at the critical load. Figures 9–11 show prebuckled deflection shape to be significantly different from the shape of the postbuckle. The analytical prebuckled contours resemble the moiré data provided by Wilkins [22,23], as shown in Fig. 9. Behavior similar to that shown in Figs. 9–11 was reported by Knight et al. [36]. Knight et al. tested a 16-ply angle-ply (±45) laminated shell panel and they reported both numerical and experimental results showing pre- and postbuckled shapes similar to that shown here. Figure 9 also shows the panel response using the higher-order MR nonlinearity to be similar to the VK response.

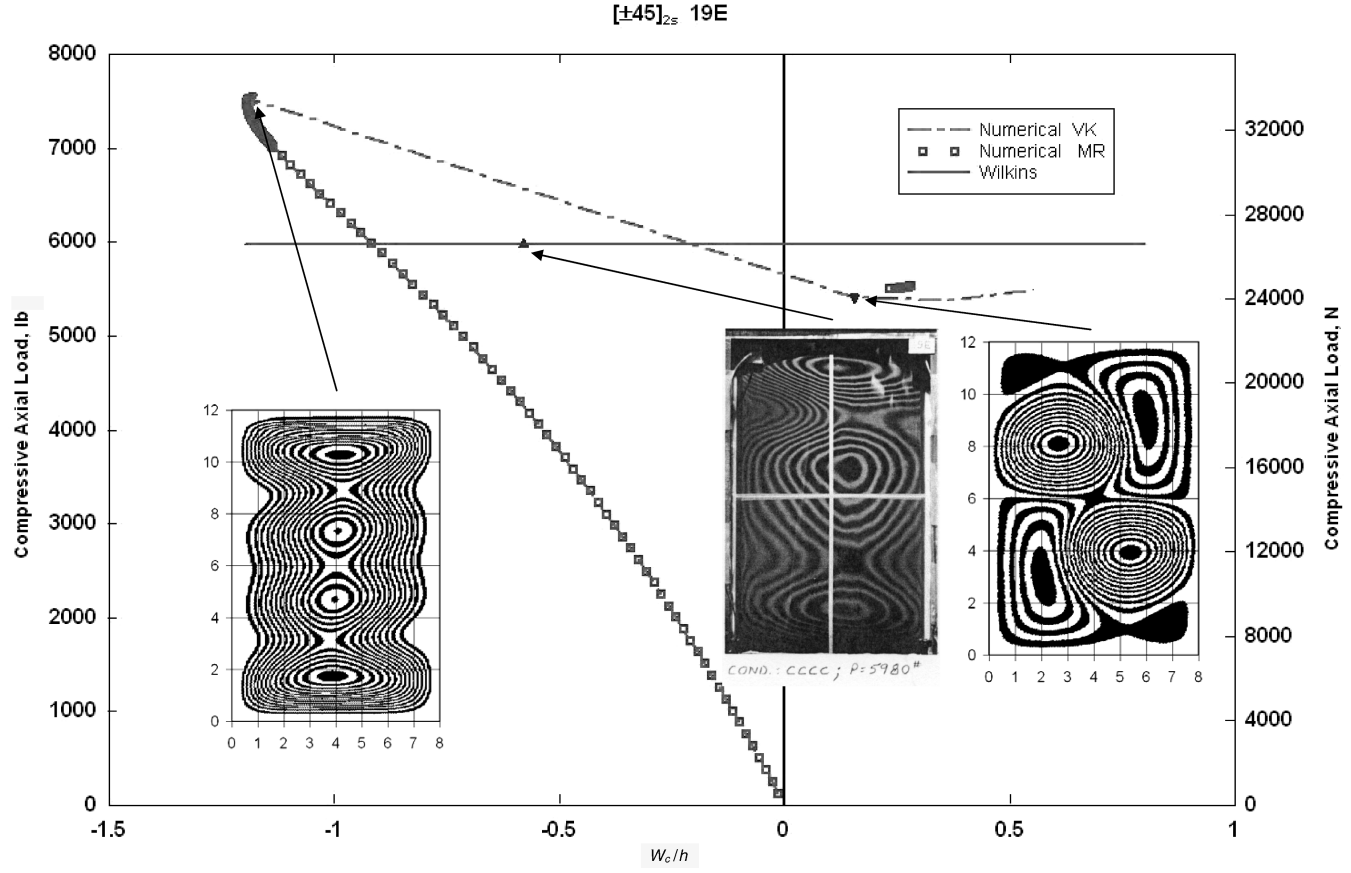

Fig. 9 Numerical center panel deflection vs axial load and Wilkins experimental results ($h = 0.0598$ in. $= 1.52$ mm). Numerical contour plot on the far right has approximately 0.02 in. (0.51 mm) per fringe. Numerical instability occurs at $P = 7550$ lb (33,580 N) compared with 5980 lb (26,600 N) reported by Wilkins.

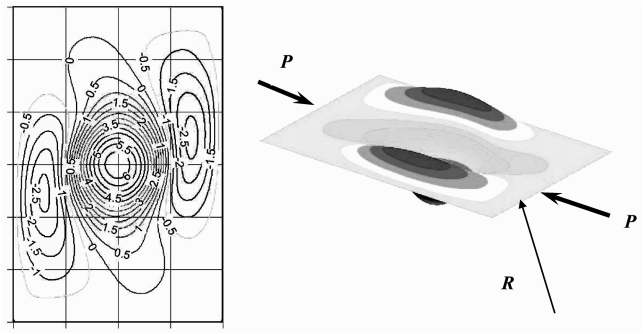

Fig. 12 Full-field panel deflection (w/h) for the unidirectional laminate $[-30]_{2s}$. Center panel deflects inward, that is, toward the panel center of curvature.

4. $[-30]_{2s}$ Wilkins Panel 37A

Figures 12 and 13 give the response of the $[-30]_{2s}$ laminate. Similar to that seen in the angle-ply laminate, the initial center panel deflection is away from the center of curvature but reverses direction as the buckling load approaches. The postbuckled response shows large deflections toward the center of curvature ($w_c/h \approx 6$) (see Fig. 12). The MR response is similar to the VK and is also shown in Fig. 13. The full-field panel response shown in both figures resembles the moiré data provided by Wilkins [22,23].

5. Panel Summary

The nonlinear response of four cylindrical laminated panels was examined and the results are summarized in Table 2. The column on the far right of the table gives the analytical prediction of the buckling load as reported by Wilkins [22,23]. The Wilkins theoretical value is based on a classical linear buckling analysis assuming Vlasov shell theory, small displacements, and no transverse shear deformation. The present approach consistently gives critical loads closer to the experimental. Actual imperfections in the Wilkins panels could explain, in part, the consistently lower experimental buckling loads. Wilkins reports panel thickness mean deviations of approximately 5%.

V. $[0/90]_T$ Cylindrical Panels

Numerical simulations for unsymmetrically laminated cross-ply cylindrical panel geometries subjected to axial compression show the effect of the MR nonlinearity vs the simpler VK nonlinearity. The panel loading and boundary conditions are similar to that of the Wilkins panels of the last section (see Fig. 3). The panel geometry is given in the figure captions. The curvature parameter Z is defined in Eq. (30) for a cylindrical panel [37].

$$Z = (2a)^2/Rh \tag{30}$$

where a, R, and h are defined in Fig. 1. For a constant curvature parameter, R and h can be varied to get geometries considered thin (large a/h) and thick (small a/h).

Figures 14 and 15 show nondimensional load λ vs normalized center panel deflection for a flat plate ($Z = 0$) and a cylindrical panel ($Z = 10$). In both cases for the thin geometry, the VK and the MR approaches give a very consistent response, as expected. In both cases, the thick geometry gives a lower nondimensional critical load (approximately where w_c/h increases rapidly for a small increase in axial compression) vs the thin geometry. For thick geometries, the VK nonlinearity response is characterized by an increasing center panel deflection with load. However, for larger λ, the MR response diverges from the VK solution and is indicative of a stiffer response. The plots also indicate the MR solution may carry a larger maximum load vs the VK solution for the thick case. The plots also show that the critical load is higher for the curved panel compared with the flat plate.

VI. Conclusions

A small-strain, elastic, geometrically nonlinear shell approach applicable to doubly curved laminated panels with arbitrary ply orientation stacking was developed. The approach captures parabolic transverse shear strain and, therefore, stress through the shell thickness. Moderate rotation geometric nonlinearity in the shell strain-displacement relations was described. Retention of terms of the second order and larger gives a von Kármán type nonlinearity in which the in-plane strains are nonlinear and the transverse shear strains are linear in displacement. Keeping terms of the third order and larger results in a moderate rotation approach in which both the

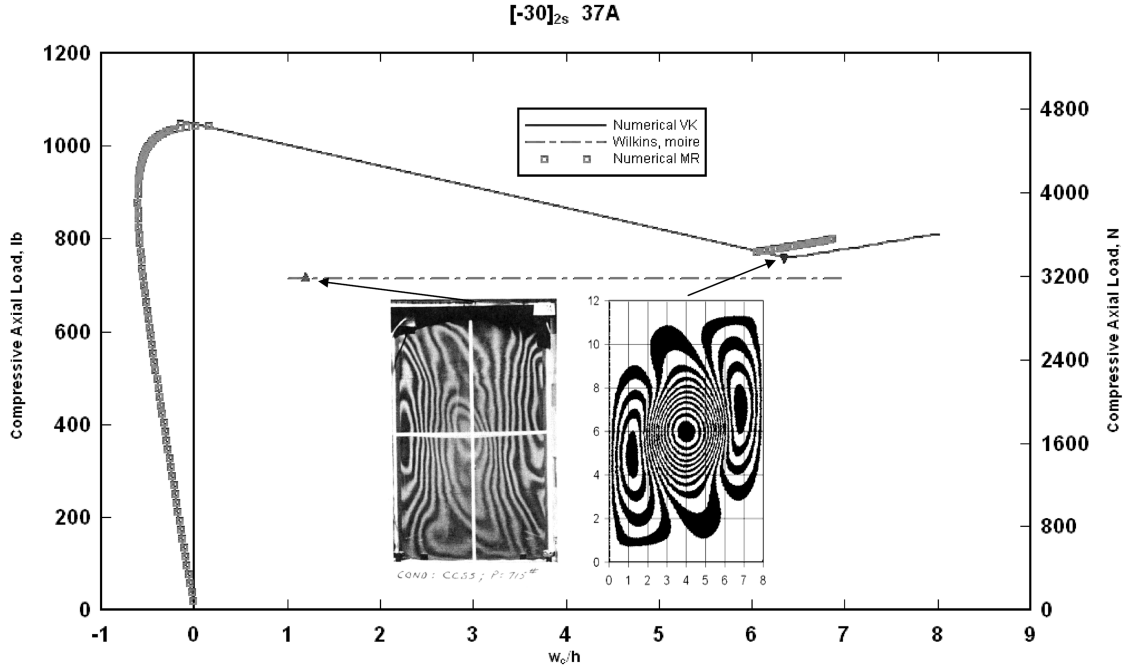

Fig. 13 Numerical center panel deflection vs axial load and Wilkins experimental results ($h = 0.0282$ in. $= 0.72$ mm). Numerical contour plots are from the 100 × 100 mesh and each fringe represents approximately 0.02 in. (0.51 mm) of deflection. Numerical buckling occurs at approximately 1055 lb (4693 N) compared with 715 lb (3180 N) from the moiré data.

Table 2 Cylindrical panel summary

Laminate	Panel no. boundary condition	Numerical maximum load, lb	Wilkins experimental moiré/Southwell, lb	Wilkins theoretical, lb
$[0/90]_s$	21A CCSS	1250	985/1125	1530
$[0]_{6s}$	47B CCSS	N/A	18,000/19,598	20,600
$[0]_{6s}$	47B CCCC	N/A	20,560/21,538	N/A
$[\pm 45]_{2s}$	19E CCCC	7554	5980 (moiré)	9500
$[-30]_{2s}$	37A CCSS	1055	715 (moiré)	2200

in-plane and the transverse strain-displacement relations are nonlinear. The approach was tested by comparisons with the extensive experimental results of Wilkins [22,23]. Axially compressed laminated cylindrical panels experienced a critical load without aid of numerical imperfections. The higher-order MR nonlinearity and the VK-type nonlinearity gave a consistent panel response for those cases examined. That is, due to symmetrical lamination stacking and thin geometries, the additional nonlinearities in the transverse shear degrees of freedom were not important. The present numerical approach gives reasonable-to-good comparisons to the Wilkins experimental results, although critical panel loads are too high compared with the experimental results. Panel contours compare reasonably with Wilkins's moiré full-field panel response. The buckled shape of each panel compares well with the experimental, although the numerical typically shows greater deflections than that seen in the moiré response. The nonlinear response of unsymmetrically laminated, thicker, cross-ply shell geometries shows the influence of the additional nonlinearities of the MR approach. The MR nonlinearity gives a stiffer panel response vs the VK approach.

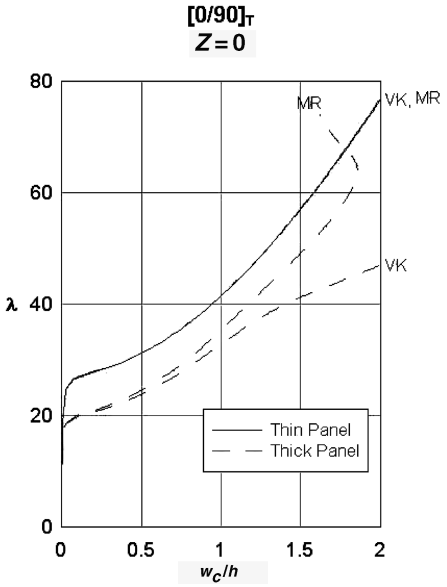

Fig. 14 Flat-plate nondimensional load vs normalized center panel deflection. (Thin plate $2a = 2b = 10$ in. and $h = 0.1$ in. Thick plate $2a = 2b = 10$ in. and $h = 1$ in.)

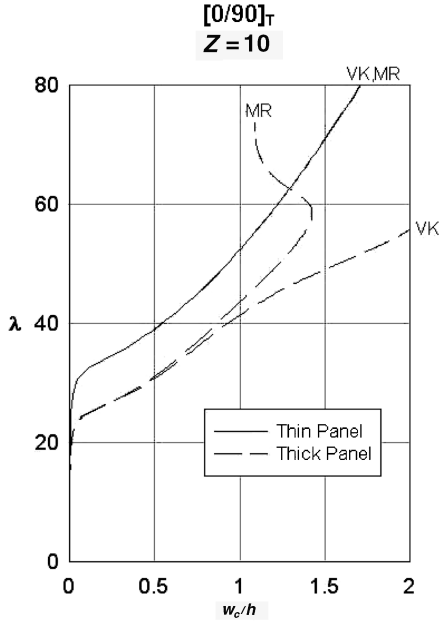

Fig. 15 Curved panel nondimensional load vs normalized center panel deflection. (Thin panel $2a = 2b = 10$ in., $R = 100$ in., and $h = 0.1$ in. Thick panel $2a = 2b = 10$ in., $R = 10$ in., and $h = 1$ in.)

Acknowledgments

The author gratefully acknowledges the computer support received from the Modeling and Simulation Research Center, Department of Aeronautics, U.S. Air Force Academy, Colorado, headed by Scott Morton, and the Aeronautical Systems Center Major Shared Resource Center, Wright–Patterson Air Force Base, Ohio. Also, the computer advice provided by Steven Senator is appreciated.

References

[1] Hilburger, M. W., Nemeth, M. P., and Starnes, J. H., "Shell Buckling Design Criteria Based on Manufacturing Imperfection Signatures," *AIAA Journal*, Vol. 44, No. 3, Mar. 2006, pp. 654–663.

[2] Sheinman, I., and Goldfeld, Y., "Buckling of Laminated Cylindrical Shells in Terms of Different Theories and Formulations," *AIAA Journal*, Vol. 39, No. 9, Sept. 2001, pp. 1773–1781.

[3] Tudela, M. A., Lagace, P. A., and Wardle, B. L., "Buckling Response of Transversely Loaded Composite Shells, Part 1: Experiments," *AIAA Journal*, Vol. 42, No. 7, July 2004, pp. 1457–1464.

[4] Tudela, M. A., Lagace, P. A., and Wardle, B. L., "Buckling Response of Transversely Loaded Composite Shells, Part 2: Numerical Analysis," *AIAA Journal*, Vol. 42, No. 7, July 2004, pp. 1465–1473.

[5] Weaver, P. M., "On Beneficial Anisotropic Effects in Composite Structures," AIAA Paper 2002-1582, 2002.

[6] Diaconu, C. G., and Weaver, P. M., "Postbuckling of Long Laminated Composite Plates with Unsymmetric Laminate Configurations," AIAA Paper 2005-1869, 2005.

[7] Schultz, M. R., and Hyer, M. W., "A Morphing Concept Based on Unsymmetric Composite Laminates and Piezoceramic MFC Actuators," AIAA Paper 2004-1806, 2004.

[8] Majeed, M. A., and Hyer, M. W., "Mechanical Behavior of Inplane-Loaded Unsymmetrically Laminated Plates," AIAA Paper 2005-2099, 2005.

[9] Sun, C. T., and Chin, H., "On Large Deflection Effects in Unsymmetric Cross-Ply Composite Laminates," *Journal of Composite Materials*, Vol. 22, Nov. 1988, pp. 1045–1059.

[10] Icardi, U., "The Nonlinear Response of Unsymmetric Multilayered Plates Using Smeared Laminate and Layerwise Models," *Composite Structures*, Vol. 29, 1994, pp. 349–364.

[11] Eslami, H., Park, E. S., and Gangadharan, S., "Nonlinear Analysis of Unsymmetrical Composite Laminates Using the Large Deflection First-Order Shear Deformation Theory with Arbitrary Angle of Orientation," AIAA Paper 2002-1578, 2002.

[12] Wu, C. P., and Chi, Y. W., "Three Dimensional Nonlinear Analysis of Laminated Cylindrical Shells Under Cylindrical Bending," *European*

Journal of Mechanics, A/Solids, Vol. 24, No. 5, 2005, pp. 837–856.
[13] Reddy, J. N., and Liu, C. F., "A Higher Order Shear Deformation Theory of Laminated Elastic Shells," *International Journal of Engineering Science*, Vol. 23, No. 3, 1985, pp. 319–330.
[14] Levinson, M. A., "An Accurate Simple Theory of the Statics and Dynamics of Elastic Plates," *Mechanics Research Communications*, Vol. 7, No. 6, 1980, pp. 343–350.
[15] Murthy, M. V. V., "An Improved Transverse Shear Deformation Theory for Laminated Anisotropic Plates," NASA TP-1903, Nov. 1981.
[16] Wempner, G. A., "Finite Elements, Finite Rotations, and Small Strains of Flexible Shells," *International Journal of Solids and Structures*, Vol. 5, No. 2, Feb. 1969, pp. 117–153.
[17] Zienkiewicz, O. C., Taylor, R. D., and Too, J. M., "Reduced Integration Technique in General Analysis of Plates and Shells," *International Journal for Numerical Methods in Engineering*, Vol. 3, 1971, pp. 275–290.
[18] Alwar, R. S., and Narasimhan, M. C., "Nonlinear Analysis of Laminated Axisymmetric Spherical Shells," *International Journal of Solids and Structures*, Vol. 30, No. 6, 1993, pp. 857–872.
[19] Librescu, L., "Refined Geometrically Nonlinear Theories of Anisotropic Laminated Shells," *Quarterly of Applied Mathematics*, Vol. 45, Apr. 1987, pp. 1–22.
[20] Schmidt, R., and Reddy, J. N., "A Refined Small Strain and Moderate Rotation Theory of Elastic Anisotropic Shells," *Journal of Applied Mechanics*, Vol. 55, Sept. 1988, pp. 611–617.
[21] Dennis, S. T., and Palazotto, A. N., "Large Displacement and Rotational Formulation for Laminated Shells Including Parabolic Transverse Shear," *International Journal of Non-Linear Mechanics*, Vol. 25, No. 1, 1990, pp. 67–85.
[22] Wilkins, D. J., "Compression Buckling Tests of Laminated Graphite-Epoxy Curved Panels," AIAA Paper 74-32, Feb. 1974.
[23] Wilkins, D. J., "Anisotropic Curved Panel Analysis, General Dynamics," Convair Aerospace Division, Rept. FZM-5567, May 1973.
[24] Love, T. S., and Brubaker, W. R., "Advanced Composites: Buckling, Pressure, and Natural Frequency Tests on Curved Panel Components," General Dynamics Test Lab., Rept. FSG-739, Dec. 1971.
[25] Saada, A. S., *Elasticity Theory and Applications*, Pergamon, Oxford, England, U.K., 1974.
[26] Novozhilov, V. V., *Foundations of the Nonlinear Theory Of Elasticity*, Graylock, Rochester, NY, 1953.
[27] Jones, R. M., *Mechanics of Composite Materials*, McGraw–Hill, New York, 1975.
[28] Palazotto, A. N., and Dennis, S. T., *Nonlinear Analysis of Shell Structures*, AIAA Education Series, AIAA, Washington, D.C., 1992.
[29] Gropp, W., Lusk, E., and Skjellum, A., *Using MPI, Portable Parallel Programming with the Message Passing Interface*, MIT Press, Cambridge, MA, 1999.
[30] Golub, G., and Ortega, J. M., *Scientific Computing an Introduction with Parallel Computing*, Academic Press, New York, 1993.
[31] Anon., "SGI Origin 3900 User's Guide," *Aeronautical Systems Center Major Shared Resource Center* [online database], http://www.asc.hpc.mil [cited Sept. 2003].
[32] Reddy, J. N., Chandraskekhara, K., and Chao, W. C., "Geometrically Nonlinear Analysis of Laminated Elastic Structures," NASA CR 191055, Jan. 1993.
[33] Wardle, B. L., "The Incorrect Benchmark Shell Buckling Solution," AIAA Paper 2006-2028.
[34] Dally, J. W., and Riley, W. F., *Experimental Stress Analysis*, McGraw–Hill, New York, 1978.
[35] Timoshenko, S. P., and Gere, J. M., *Theory of Elastic Stability*, McGraw–Hill, New York, 1961.
[36] Knight, N. F., Starnes, J. H., and Waters, W. A., "Postbuckling Behavior of Selected Graphite-Epoxy Cylindrical Panels Loaded in Axial Compression," AIAA Paper 86-0881, 1986.
[37] Leissa, A. W., "Buckling of Laminated Composite Plates and Shell Panels," Air Force Wright Aeronautical Labs. Rept. TR-85-3069, June 1985.

A. Palazotto
Associate Editor